SCISPACE
formerly Typeset

Open access • Proceedings Article • DOI:10.1117/12.437025

Modeling of LWIR Hyperspectral System Performance for Surface Object and Effluent Detection Applications — Source link

John P. Kerekes, Michael K. Griffin, Jerrold E. Baum, Kristine E. Farrar

Institutions: Massachusetts Institute of Technology

Published on: 20 Aug 2001 - Proceedings of SPIE (International Society for Optics and Photonics)

Topics: Radiance, Hyperspectral imaging and Emissivity

Related papers:

- Full-spectrum spectral imaging system analytical model
- Full spectrum modeling of at-sensor spectral radiance variability due to surface variability
- Atmospheric radiance interpolation for the modeling of hyperspectral data
- Atmospheric correction of airborne infrared hyperspectral images by direct estimation of the radiative terms
- Background Radiance Estimation for Gas Plume Quantification for Airborne Hyperspectral Thermal Imaging

Share this paper:

View more about this paper here: https://typeset.io/papers/modeling-of-lwir-hyperspectral-system-performance-for-47paon6y30

Modeling of LWIR Hyperspectral System Performance for Surface Object and Effluent Detection Applications*

John P. Kerekes#, Michael K. Griffin, Jerrold E. Baum, Kristine E. Farrar
Lincoln Laboratory, Massachusetts Institute of Technology

ABSTRACT

In support of hyperspectral sensor system design and parameter tradeoff investigations, an analytical end-to-end remote sensing system performance forecasting model has been extended to the longwave infrared (LWIR). The model uses statistical descriptions of surface emissivities and temperature variations in a scene and propagates them through the effects of the atmosphere, the sensor, and processing transformations. A resultant system performance metric is then calculated based on these propagated statistics.

This paper presents the theory and operation of extensions made to the model to cover the LWIR. Theory is presented on combining both surface spectral emissivity variation with surface temperature variation on the upwelling radiance measured by a downward-looking LWIR hyperspectral sensor. Comparisons of the model predictions with measurements from an airborne LWIR hyperspectral sensor at the DoE ARM site are presented. Also discussed is the implementation of a plume model and radiative transfer equations used to incorporate a thin man-made effluent plume in the upwelling radiance. Example parameter trades are included to show the utility of the model for sensor design and operation applications.

Keywords: LWIR hyperspectral system modeling, sensor parameter tradeoffs, effluent detection

1. INTRODUCTION

Hyperspectral imaging (HSI) systems operating in the reflective solar portion of the optical spectrum (0.4 to 2.5 μm) have demonstrated utility in a variety of applications ranging from environmental monitoring to subpixel object detection[1,2]. The limiting requirement of solar illumination for these systems has motivated development of thermal infrared hyperspectral systems with the hope of achieving similar utility but with a day/night capability. Also, since some materials (particularly man-made effluents) have stronger and more distinct spectral features in the longwave infrared, LWIR systems offer the possibility of additional applications for which hyperspectral sensing can be used.

Previously, an end-to-end reflective solar hyperspectral remote sensing system model had been developed using an analytical framework[3]. This model, known as Forecasting and Analysis of Spectroradiometric System Performance (FASSP), has been used for sensitivity studies and requirements analysis for systems operating in the VNIR/SWIR portion of the spectrum. This paper presents several enhancements to the model, which extend its capability to systems operating in the longwave infrared.

2. FASSP MODEL STRUCTURE

The fundamental underlying premise of the FASSP model is that the various classes of materials in a scene can be adequately represented in a statistical fashion by their first- and second-order spectral statistics. The model uses as an input the mean vectors and covariance matrices of the spectral reflectance (1 – emittance) of each material class. These means and covariances are propagated through the imaging and processing chain to provide an estimate of system performance. Figure 1 provides a conceptual block diagram for this process.

In Figure 1, the surface spectral (reflectance or emittance) statistics are transformed to spectral radiance statistics through linear functions of atmospheric radiative transfer functions. These radiance statistics are then further transformed by linear operations of the sensor including channel spectral response functions, and fixed and random sensor errors. The sensor output statistics are then transformed through user-selectable processing functions to result in a performance metric such as spectral

* This work was sponsored by the Department of Defense under contract F19628-00-C-0002. Opinions, interpretations, conclusions, and recommendations are those of the author and not necessarily endorsed by the United States Air Force.
# kerekes@ll.mit.edu; phone (781) 981-0805; fax (781) 981-7271; MIT Lincoln Laboratory, 244 Wood St., Lexington, MA 02420-9108

Algorithms for Multispectral, Hyperspectral, and Ultraspectral Imagery VII, Sylvia S. Shen, Michael R. Descour, Editors, Proceedings of SPIE Vol. 4381 (2001)
© 2001 SPIE · 0277-786X/01/$15.00

characterization accuracy, or a probability of detection vs. false alarm curve (P_D/P_{FA}). Our previous work[3] described in detail the equations used to propagate the statistics to obtain a performance metric for the reflective solar part of the spectrum.

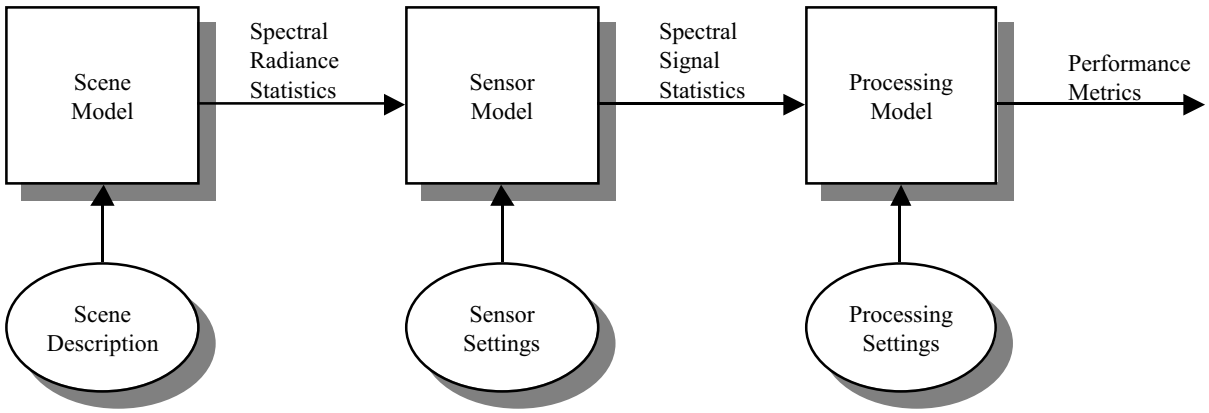

Figure 1. Block diagram of the FASSP model structure.

3. LWIR ENHANCEMENTS

Enhancements to the FASSP model to extend its operation into the LWIR have been made in three general areas. The first was in developing the equations to combine the surface emissivity and temperature effects with the radiative transfer equations to obtain the scene spectral radiance mean and covariance. Another was the incorporation of a plume model and the radiative transfer modeling to predict radiances for man-made effluents. The third was to implement models for LWIR sensors including additional noise effects in detectors operating in that spectral region. The following subsections describe these enhancements.

3.1 LWIR Spectral Radiance Modeling

The FASSP scene radiance model considers a scene to consist of one or more background classes and one target class. Each class is defined by the fraction of the scene occupied by that class and a set of statistics. The target class is considered to be subpixel or at most occupy a single pixel. The LWIR statistics for each class include the mean temperature $\bar{T}$, the temperature variance σ_T^2, the mean spectral emissivity $\bar{\varepsilon}_\lambda$, and the full spectral emissivity covariance matrix Σ_ε. The following sections describe how these surface statistics are transformed into at-sensor radiance statistics. Note: in this initial LWIR model, only a single background is assumed.

3.1.1 Mean Spectral Radiance

The at-sensor spectral radiance has three terms in the LWIR as shown in equation (1). The first represents the surface emitted radiance, the second is the reflected downwelling radiance, and the third is the atmospheric emitted upwelling radiance.

$$L_{\lambda,Sensor} = \tau_\lambda \varepsilon_\lambda B_\lambda(T) + \tau_\lambda (1-\varepsilon_\lambda) L_{\lambda,Down} + L_{\lambda,Up} \quad (1)$$

Where,

τ_λ = atmospheric transmittance from the surface to the sensor,
ε_λ = surface spectral emissivity,
$B_\lambda(T)$ = Planck radiance function for temperature T,
$L_{\lambda,Down}$ = atmospheric emitted downwelling radiance, and
$L_{\lambda,Up}$ = atmospheric emitted upwelling radiance.

The various components are computed using the Air Force Research Laboratory's MODTRAN[4] radiative transfer code, or simply through the Planck radiance equation. The spectral radiances for the target and background are computed using separate MODTRAN runs with the appropriate mean surface emissivity and mean temperature. For subpixel targets with subpixel fraction *f*, these components are linearly combined as in equation (2).

$$L_{\lambda,Sensor,Total} = f L_{\lambda,Sensor,Target} + (1-f) L_{\lambda,Sensor,Background} \quad (2)$$

3.1.2 Spectral Radiance Covariance

The at-sensor spectral radiance covariance matrix was derived by computing the expectation of the scene radiance defined in equation (1) with the mean subtracted times the transpose of that quantity as shown in equation (3).

$$\Sigma_{\lambda,Sensor} = E\{[L_{\lambda,Sensor} - \overline{L}_{\lambda Sensor}][L_{\lambda,Sensor} - \overline{L}_{\lambda Sensor}]^T\} \quad (3)$$

In the derivation, an assumption was made that the surface temperature of the object is uncorrelated with its spectral emissivity. This is not strictly true, as thermal cooling is dependent upon emissivity (among other parameters) and emissivity is often related to the solar albedo which can govern the object's temperature during the day. However, these assumptions make the computations tractable and are not seen as overly restrictive to adequately characterize the variability in the spectral radiance. The resultant expression has six terms as shown in equation (4) for whole pixel objects. All terms are *NxN* where *N* is spectral dimensionality of the data.

$$\begin{aligned}\Sigma_{Sensor} = \mathrm{T}[&\Lambda_{\sigma_L}\Sigma_{\varepsilon_S}\Lambda_{\sigma_L} + \Lambda_{\overline{L}_S}\Sigma_{\varepsilon_S}\Lambda_{\overline{L}_S} + \Lambda_{\overline{\varepsilon}_S}\Sigma_{L_S}\Lambda_{\overline{\varepsilon}_S} + \\ &\Lambda_{L_D}\Sigma_{\varepsilon_S}\Lambda_{L_D} - (\Lambda_{L_D}\Sigma_{\varepsilon_S}\Lambda_{\overline{L}_S} + \Lambda_{\overline{L}_S}\Sigma_{\varepsilon_S}\Lambda_{L_D})]\mathrm{T}\end{aligned} \quad (4)$$

Where,

- T = diagonal matrix of surface-to-sensor atmospheric transmittance,
- Λ_{σ_L} = diagonal matrix of surface emitted spectral radiance standard deviation with each entry $\sigma_L = \sigma_T \partial B/\partial T$ for $T = \overline{T}$, where σ_T is the surface temperature standard deviation and $\partial B/\partial T$ is the derivative of the Planck radiance function,
- Σ_{ε_S} = full spectral emissivity covariance matrix,
- $\Lambda_{\overline{L}_S}$ = diagonal matrix of mean Planck radiance emitted by the surface (assumes black body surface),
- Σ_{L_S} = spectral covariance of surface emitted radiance(= $\Lambda_{\sigma_L}[1]\ \Lambda_{\sigma_L}$, where [1] is a *NxN* matrix of ones) ,
- $\Lambda_{\overline{\varepsilon}_S}$ = diagonal matrix of mean surface emissivity,
- Λ_{L_D} = diagonal matrix of downwelling radiance.

For subpixel targets, the whole pixel covariances are weighted by a function of the target subpixel fraction as in equation (5).

$$\Sigma_{Sensor,Total} = f^2\Sigma_{Sensor,Target} + (1-f)^2\Sigma_{Sensor,Background} \quad (5)$$

3.2 Effluent Modeling

The case of a layer in the atmosphere with an enhanced amount of trace, or man-made gas, is modeled in FASSP through a two step process. First, a column concentration is produced by a plume model which takes into account effluent emission characteristics and meteorological parameters. Second, this concentration is used in radiative transfer equations to modify the scene radiance statistics to include the effects of the effluent. The following two subsections describe these steps. A companion paper in this proceedings[5] provides additional details and examples.

3.2.1 Plume Modeling

The plume model used in FASSP is a Gaussian-plume dispersion model that calculates short-term pollutant concentrations from a single point source at a user-specified receptor grid in level or gently rolling terrain[6]. It is applicable to locations where a single wind vector for each hour is a reasonable approximation of the flow over the source area considered. Briggs' plume-rise equations[7] are used to estimate the effective height of the point source. Concentrations are determined using distance crosswind and distance upwind from the receptor to the source. Inputs to the model are a set of user-specified options, source parameters, meteorological data, and receptor information.

For model execution, the user specifies parameters and options needed for the application. Options are included for the treatment of stack-tip downwash, gradual plume rise, and buoyancy-induced dispersion[8]. The user also specifies the characteristics of emission sources and meteorological inputs. Plume model inputs include stack information such as emission rate and stack height, diameter, gas temperature and gas exit velocity. Meteorological parameters (anemometer

height, stability class, wind speed and direction, air temperature and mixing height) must be present for each simulation hour. The increase of wind speed with height is included, based upon a power-law wind profile. The power-law exponent is dependent upon the stability classification and surface roughness[9]. There is no inclusion of directional shear with height. This means that the direction of flow is assumed to be the same at all levels over the region.

On output, the model produces vertically integrated gas concentrations C (g m^{-2}) at each receptor grid location. The model assumes a steady state condition and can be used for short-term (one hour to one day) determination of urban air quality resulting from pollutants released from a single source. This version of the plume model is most applicable for pollutants that are quite stable chemically and physically. Selective removal or reaction at the plume-ground interface or dependence upon concentration levels may not be well handled by the model.

The concentrations C are converted to units of molecules cm^{-2} (values easily incorporated into the radiative transfer model described in the next subsection) using the following equation,

$$C\left(\, molecules\ cm^{-2}\right) = \frac{A}{M}\left(10^{-4}\right) \times C\left(\, g\ m^{-2}\right), \tag{6}$$

where A is Avogadro's number (6.02297×10^{23} molecules $mole^{-1}$) and M is the gas molecular weight (g $mole^{-1}$). Figure 2 shows a plot of the two dimensional effluent concentration for locations downwind of a source, approximately 1 hour after the first emission from the stack. The plot is limited to a 100m x 60m area and is for an SO_2 gas emission rate of 3.85 g sec^{-1}.

As the effluent dissipates downwind from the source, the temperature of the gas also changes as it mixes with the ambient air. Eventually, the temperature of the gas reaches the ambient temperature, presumably when the local concentration of the gas reaches the ambient or background concentration value. Therefore, an assumption is made that the ratio of the effluent temperature at some location downwind of the stack to the effluent temperature at the stack is proportional to the ratio of the effluent concentration at that location to the maximum concentration. Using this relationship, it is simple to derive a grid of effluent temperatures. Since vertically-integrated concentration values are computed, it is assumed that the temperature corresponds to a layer representative of the peak concentration (possibly at or near the height of the stack).

For the current implementation of FASSP, only a single value representative of the maximum concentration of effluent and the associated effluent temperature (usually the effluent temperature at the stack) is used. These are the only values that are passed from the plume model to the radiative transfer code at this time.

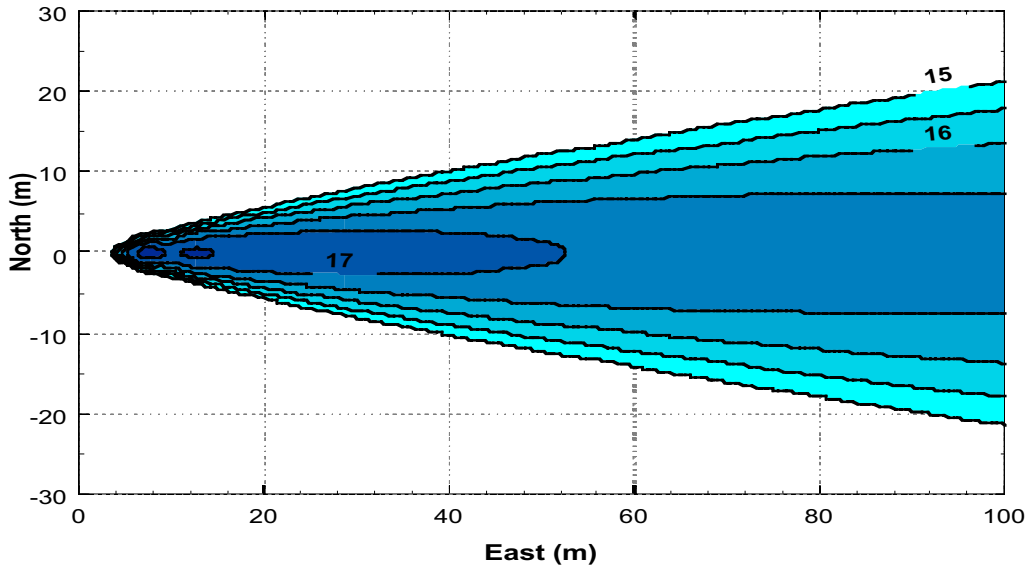

Figure 2. Plot of the effluent concentration after one hour as a function of distance (m) east and north of the source. Values are shown as $\log_{10}$ of the concentration in molecules cm^{-2}. Ambient concentration is 10^{15} molecules cm^{-2}.

3.2.2 Effluent Radiative Transfer

The technique used to model the spectral radiance from a scene containing a plume layer consists of the following steps: 1) obtain the peak vertically-integrated concentration from the Gaussian-plume model; 2) compute layer optical depths using a line-by-line model such as FASE[10] for atmospheric conditions approximating the plume-free scene conditions; 3) merge the spectral absorptivity of the selected effluents into the model plume layer; and 4) compute the atmospheric at-sensor radiance components. Step 1 was described above; a brief description of steps 2 - 4 follows.

Using atmospheric properties appropriate to the desired model parameters, FASE is run to produce optical depths at user-defined layers. Since only atmospheric parameters were calculated, no input surface information was needed. This approach allowed the definition of surface parameters at the time of the final radiance component calculation, without the need to rerun the line-by-line model. The full resolution layered optical depths were then degraded to a resolution of 0.1 cm^{-1}.

The characterization of the plume layer was done following the FASE calculations of the layered atmospheric optical depths. The effluent concentration was derived from the Gaussian-plume model. The effluent library contains the absorptivity as a function of wavelength and integrated gas amount (in PPM-m) for each effluent. Using the known effluent emission rate (in g s^{-1}) and the estimated gas amount from the plume model, it is relatively easy to determine the corresponding spectral absorptivity of the gas to place into the plume layer. In fact, multiple gases can be merged together using individual emission rates and spectral absorptivities to obtain a plume layer representative of a simultaneous release of many gases. For these cases, it is assumed that a single temperature was representative of all gases in the plume for a specific location away from the stack. Also, the spectral resolution of the effluent absorbances differs from the FASSP LWIR model spectral resolution. A cubic spline interpolation scheme was employed to convert the absorbances to the FASSP model resolution.

A simple radiative transfer code was developed to utilize the computed layered transmittance information along with known atmospheric temperature profiles and modeled surface temperature and emissivities to compute the upwelling, downwelling, and surface emission components of the atmospheric radiative transfer. These components are computed for cases with and without a plume. The assumption of a non-scattering (emission and absorption only) plane-parallel atmosphere was used to simplify the computations.

3.3 LWIR Sensor Modeling

The sensor model in FASSP describes the effects of an imaging spectrometer on the spectral radiance mean $\overline{L}$ and covariance Σ_L statistics of a scene. For each target and background(s) class, the input radiance statistics of every spectral channel are modified by electronic gain, radiometric noise sources, and relative calibration error to produce radiance signal statistics $\overline{S}$ and Σ_S. These signal statistics represent the scene as imaged by the spectrometer. The current FASSP model includes radiometric effects, but not spatial or spectral sources of error.

The mean scene radiance is affected only by a gain parameter. All other noise processes modify the diagonal elements of the spectral covariance matrix. The off-diagonal elements remain unchanged because it is assumed there is no channel-to-channel correlation among the noise sources.

Sensor models have been developed for both a prism spectrometer and a Fourier Transform Spectrometer (FTS). The following provides details on those models.

3.3.1 Prism Spectrometer

The generic prism spectrometer model covers the LWIR with typically a few hundred spectral channels and includes approximations for the spectral response functions and radiometric noise sources.

The radiometric noise processes occur in the detector and in the electronics (see Figure 3). Noise sources arising from the detector include photon (or shot) noise, excess low frequency noise (ELFN), and thermal noise. The noise processes originating in the electronics include quantization noise, bit errors (in recording or transmitting the data), and noise arising within the detector itself.

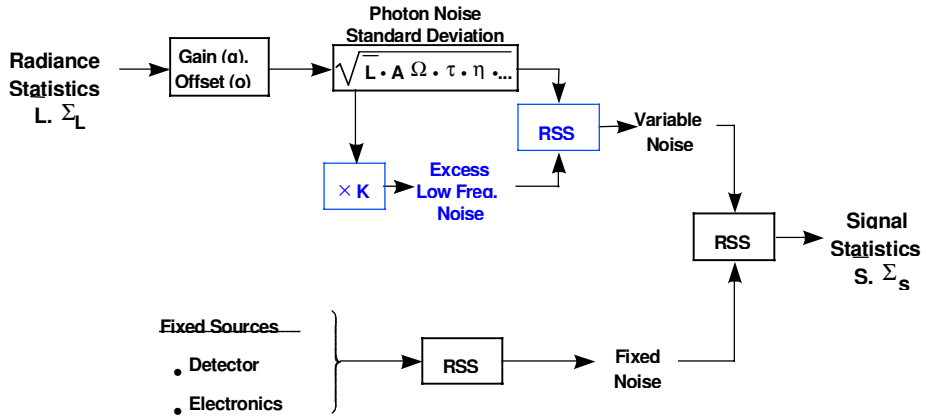

Figure 3. Block diagram of the FASSP LWIR prism spectrometer sensor model.

All of these sources are treated as independent of the input radiance, except the shot noise and ELFN. This latter type is characteristic of Si:As BIB detectors used in a number of LWIR sensors. It was recognized in the mid-1980's that, under certain conditions, BIB detectors exhibit a noise level higher than that expected just from shot noise. This 'excess' noise occurs at low frequencies and intermediate infrared backgrounds. The excess low-frequency noise does not have 1/f characteristics and is caused by processes internal to the detector. This noise mechanism limits the amount by which signal-to-noise (SNR) can be improved by co-adding frames. ELFN can be modeled as a multiplier, called the 'excess noise factor,' K, of the photon noise. Thus, ELFN increases as photon irradiance increases.

The photon, or shot, noise is a function of, among other variables, the optical transmittance and quantum efficiency. The particular values used in the model for these variables vary from sensor to sensor and are often spectrally varying as well.

There is some amount of thermal self-radiation from a typical instrument, which can not be shielded from the detector. The noise due to this radiation is combined with other fixed detector noise sources into a single value.

The noise levels predicted by the model depend upon the scene and collection parameters, but typically are in the 0.3 to 0.6 $\mu W/cm^2$-sr-μm range, which is consistent with observed noise characteristics[11].

3.3.2 Fourier Transform Spectrometer

A Fourier Transform Spectrometer has a number of noise sources that are the same as those found in grating or prism spectrometers: photon, detector, and quantization noise, for example. Because the FTS is a fundamentally different instrument, however, it also has a number of unique sources of noise, such as mirror velocity errors, sampling errors, and optical jitter. Thus, a new noise model is required, which at this point only includes the dominant noise source of a well-designed instrument, detector noise. This mechanism includes interference caused both by statistical fluctuations in the conversion of photons to electrons ('photon noise') and generated by the physical characteristics of the detector material ('detector noise').

The initial version of this new noise model[12] specifies the instrument performance in terms of noise equivalent spectral radiance, or NEN_v. This value represents that radiance which would produce an output signal equivalent to the instrument noise, at each wavenumber, or equivalently, the input radiance that would produce an output signal-to-noise ratio of one. The detector NEN_v is given by

$$NEN_{v,\,\mathrm{det}} = \frac{4L}{A_o \Omega \tau_{ox} \eta_S D^*} \sqrt{\frac{A_d}{T}} \; \frac{watts}{cm^2 - sr - cm^{-1}} \tag{7}$$

where,

A_d = Detector area (cm^2)
A_o = Optical aperture area (cm^2)
D^* = Detectivity (cm - $\sqrt{Hz}$ – $watt^{-1}$)
L = Maximum optical path difference (cm) (=1/2 $\delta\nu$)
T = Integration time (sec)
η_s = Beamsplitter efficiency
Ω = Solid angle field-of-view (sr)
τ_{ox} = Transmittance of optics (excluding beamsplitter)

*D**, the specific detectivity, is the reciprocal of the noise equivalent power, normalized to unit detector area and temporal bandwidth. It is a common figure-of-merit for describing detector performance. Because the interferometer has a finite mirror stroke, the optical path difference between the two arms of the FTS has some maximum value, *L*. This finite value limits the spectral resolution $\delta\nu$ of the instrument to be

$$\delta\nu = 1 / 2L \tag{8}$$

η_s, the beamsplitter efficiency, has values between 0 and 1 and is equal to 4RT, where R and T are the reflectance and transmission, respectively, of the beamsplitter. For an ideal beamsplitter, R = T =0.5 and $\eta_s = 1$.

4. MODEL COMPARISON TO AIRBORNE LWIR HSI DATA

The model predictions of spectral radiance were compared to airborne LWIR hyperspectral. The airborne data were collected by the SEBASS[11] instrument on 27 June 1997 at the Department of Energy Atmospheric Radiation Measurements (ARM) site near Lamont, Oklahoma. The scene consisted of wheat fields, pasture, and an area where several test panels were deployed.

The model and data were compared in two ways. First, the average spectral radiance was computed from the data for one of the test panels and compared to the model prediction using ground truth emissivity spectra and estimates of the scene parameters. Second, the variability (standard deviation) of the spectral radiance over a region of the pasture was compared to the model predicted variability. Table 1 shows some of the scene parameters used in the modeling obtained from the experimental ground truth or estimated from the data characteristics.

Table 1. Scene conditions during SEBASS overflight on 27 June 1997. The surface temperature and standard deviation apply to both the calibration panel and the pasture field.

Parameter	Value
Surface mean temperature	22°C
Surface temperature σ	0.1°C
Atmospheric model	1976 US Standard
Sensor altitude	2500 ft.

4.1 Mean Spectral Radiance Comparisons

The mean spectral radiance was calculated from nine pixels centered on the "16%" calibration panel (the 16% percent refers to the visible reflectance of the panel; its LWIR emissivity varied from 0.95 to 0.98). Ground measurements of the emissivity were used in the model along with parameters shown in Table 1 above to predict the mean spectral radiance. The comparison is shown in Figure 4. The match between model prediction and data is within 5%, and differences may be explained by errors in the absolute radiometric calibration of the sensor and by differences between the model atmosphere and the real atmosphere at the time of the collect.

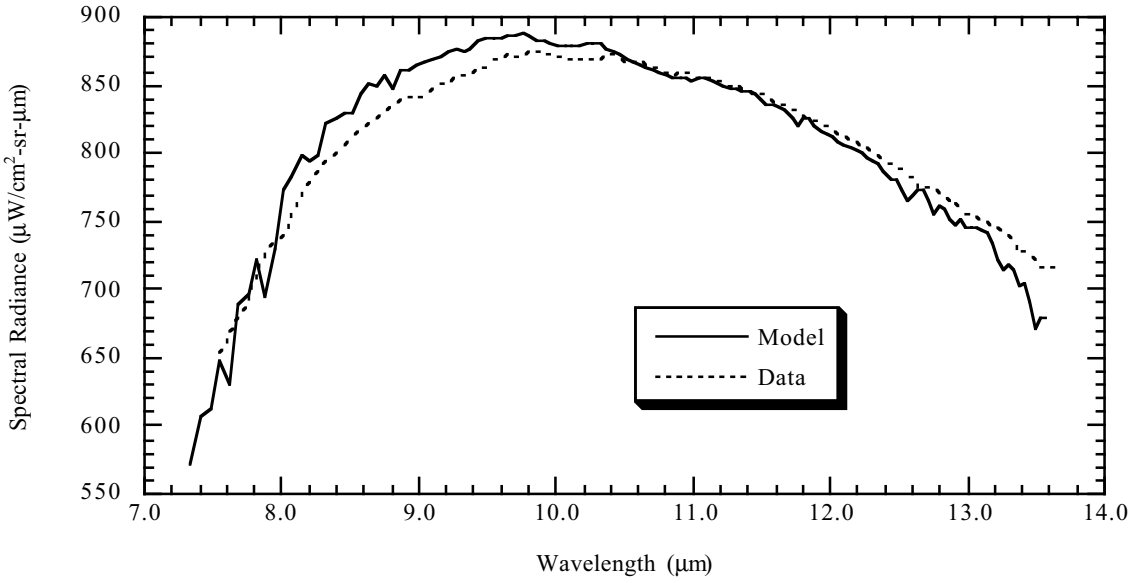

Figure 4. Comparison of the mean spectral radiance for a test panel.

4.2 Spectral Radiance Variability Comparisons

The standard deviation of the calibrated spectral radiance was calculated using one hundred pixels of the hyperspectral data over a relatively homogenous area of pasture. Since no accurate emissivity spectra of the pasture were available, a greybody mean spectrum with 0.99 emissivity was assumed, along with a standard deviation of 0.001 to represent the variability of the pasture emissivity. The pasture mean temperature and variability was as shown in Table 1. Figure 5 presents the comparison.

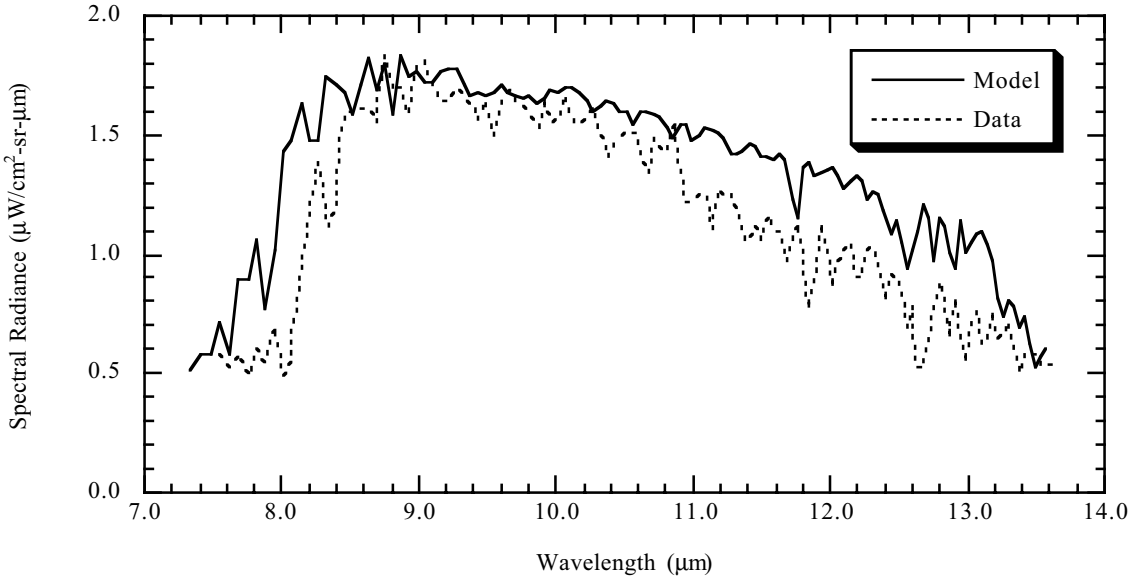

Figure 5. Comparison of the spectral radiance standard deviation for an area over the pasture.

The comparison of the variability in the sensor data to that predicted by the model shows similar overall shape and magnitude, but differences of up to 30-40% are seen. Many of the same atmospheric features are present in both the data and the model prediction, but there are some shifts seen in their peaks which may be due to spectral calibration errors in the data.

It is important to note that the variability seen in these data come from at least three sources: surface temperature variations, surface emissivity variations, and sensor noise. Examination of the relative values of these three sources in the model predictions shows the surface temperature variation dominates, with nearly the same shape and magnitude as the total variability. The sensor noise is the next largest contributor, with values around 0.5 $\mu W/cm^2$-sr-μm. The emissivity variation contribution is negligible in this case. These relative values are consistent with expectations and observed performance of the instrument. While the model seems reasonable in this case, further validation over other sites and materials will be pursued.

5. SYSTEM PARAMETER SENSITIVITIES

As an example of how this model may be used to study system parameters, an example scenario of detecting the 16% panel in a pasture field was defined. In this case, the model scenario uses the mean radiance spectra from an occurrence of the panel somewhere in the image to find it elsewhere in the image. The target is assumed to be whole pixel in all cases. Table 2 describes system parameters chosen for these sensitivity analyses.

Table 2. Baseline system parameters defined for parameter sensitivity analyses.

Parameter	Value
Target	16% calibration panel
Target mean emissivity	spectrally varying, 0.95-0.98
Target emissivity σ	0.0
Target mean temperature	23.75°C
Target temperature σ	0.1°C
Background	simulated pasture
Background mean emissivity	spectrally constant, 0.99
Background emissivity σ	0.01
Background mean temperature	22.0°C
Background temperature σ	0.1°C
Atmospheric model	1976 US Standard
Sensor	SEBASS
Sensor altitude	2500 ft.
Detection algorithm	matched filter
Spectral channels used in filter	38 between 9.0 and 11.0 μm
Constant false alarm rate	10^{-5}

Detection of the target is enabled by differences between the target and background, and is hindered by variability either in the scene or due to sensor noise. The sensitivity of detection performance was studied as a function of three different system effects as examples of how the model can be applied.

5.1 Sensitivity to Target/Background Temperature Differences

To study the effect of target/background mean temperature differences on detection performance, the background mean temperature was held constant while the target temperature was varied and detection performance recomputed. Figure 6 presents the results which show a clear minimum at a temperature difference (target-background) of 1.4°C. At this value, the combination of a higher target temperature and a lower emissivity result in nearly equal mean spectral radiances for the target and background, leading to a minimum in detection performance. Temperature differences higher or lower lead to more contrast, and thus greater detection probabilities.

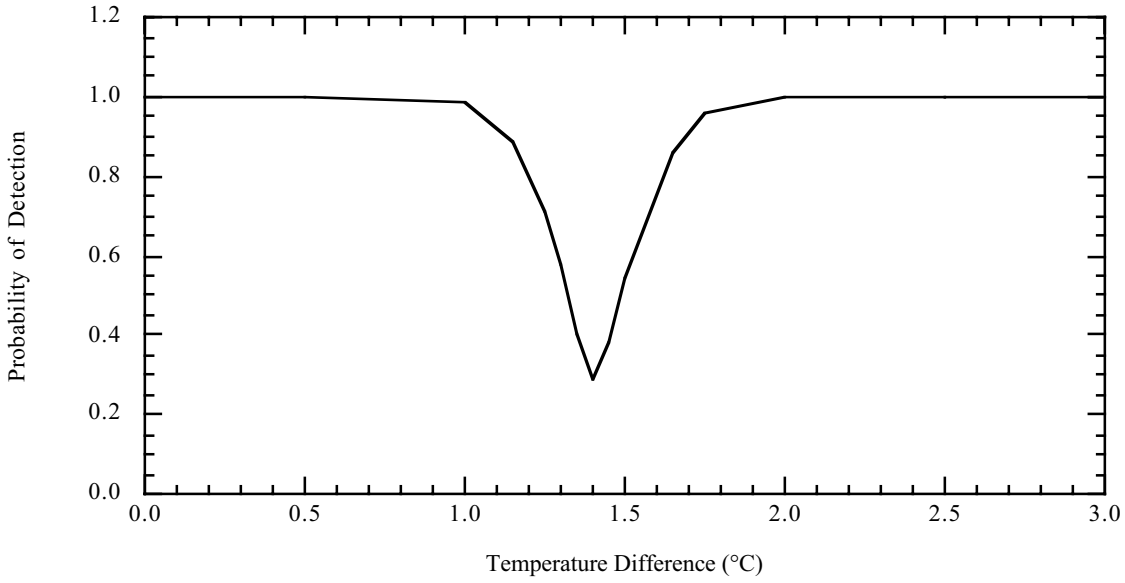

Figure 6. Detection performance sensitivity to target/background mean temperature difference for system defined in Table 2.

5.2 Sensitivity to Target Temperature Variability

To study the effect of target temperature variability, its standard deviation was varied from 0.0 to 1.0 °C while all other parameters were held constant. Figure 7 presents the results, which show the decrease in detection performance as the target temperature variability increases.

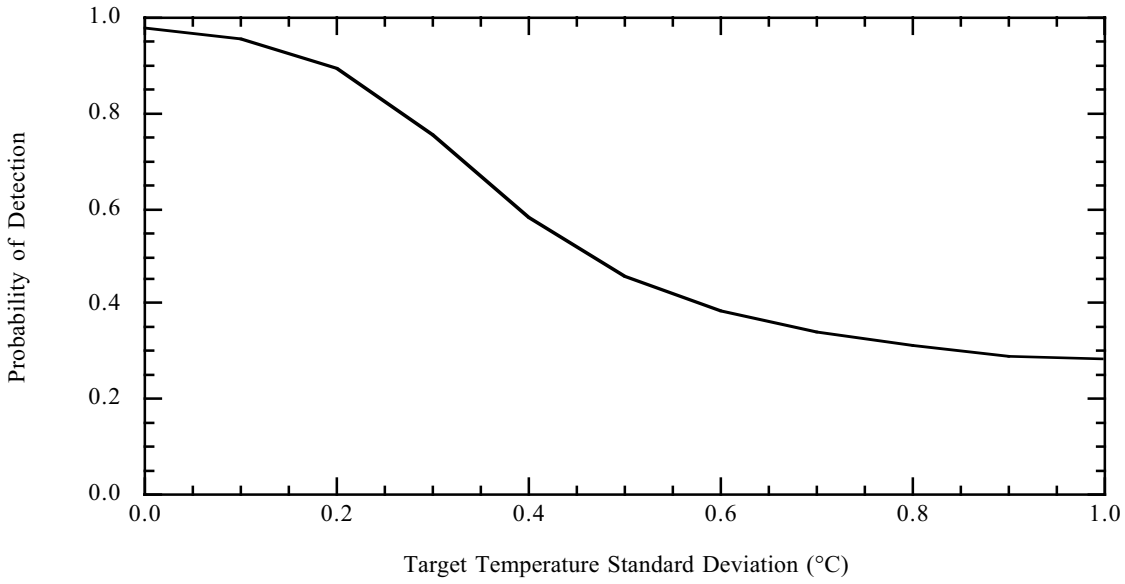

Figure 7. Detection performance sensitivity to target temperature variability for system defined in Table 2.

5.2 Sensitivity to Sensor Noise

To study the effect of sensor noise, the standard deviation of the noise was scaled by multiples from 0 to 10 while all other parameters were held constant. Figure 8 presents the fall-off in detection performance as noise increases. For the given system defined in Table 2, this result shows only modest decreases in detection probability for noise 2 to 3 times the nominal level, but significant effects when the noise is higher by an order of magnitude.

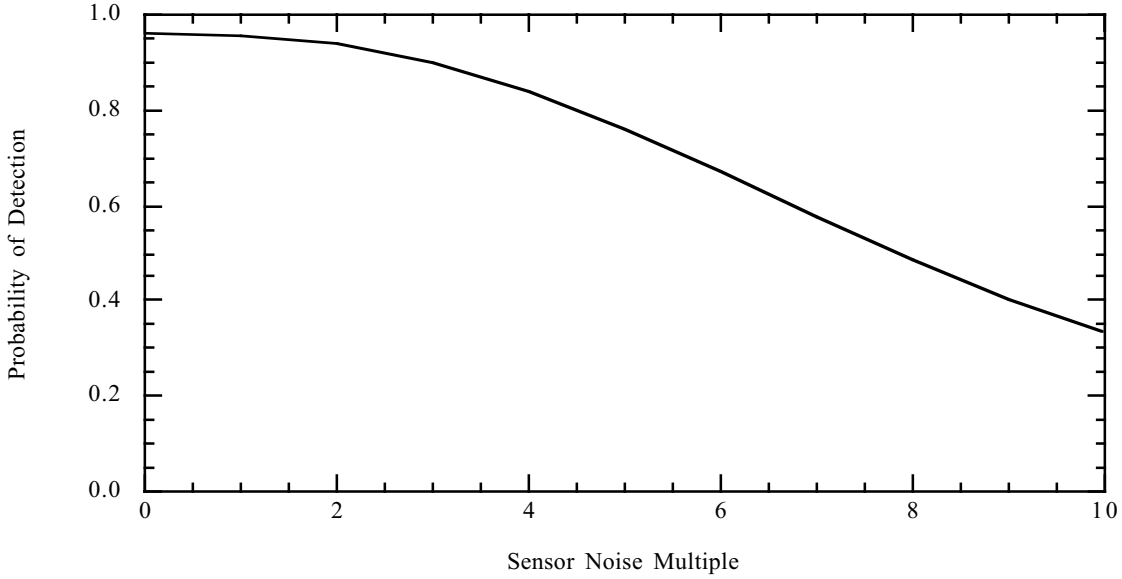

Figure 8. Detection performance sensitivity to sensor noise scaling for system defined in Table 2.

6. SUMMARY AND FUTURE WORK

Enhancements to an existing hyperspectral system performance model to extend its operation to the LWIR have been presented. The enhancements included combining the surface temperature variability with surface emissivity variability in the upwelling radiance calculation. Also included were an implementation of an effluent plume modeling capability and additions to the sensor model to include LWIR prism spectrometers and FTIR interferometers. While these enhancements have enabled the LWIR modeling of the scene and sensor portions of a remote sensing system, additional work remains to implement model representations of LWIR-specific processing algorithms. These include algorithms for LWIR atmospheric compensation to retrieve surface emissivity and temperature, and algorithms for gaseous effluent detection/identification. Also, additional validation efforts should be conducted as appropriate data sets become available.

ACKNOWLEDGMENTS

The authors would like to acknowledge the support of this work by LT Michael Rigo and the Spectral Information Technology Applications Center (SITAC), and CAPT Frank Garcia, of the Office of the Deputy Undersecretary of Defense for Science and Technology (DUSD-S&T).

REFERENCES

1. R.O. Green, editor, "Special Issue on Imaging Spectroscopy," *Remote Sensing of Environment*, **65**(3), September 1998.
2. A. E. Iverson, "Subpixel Object Detection and Fraction Estimation in Hyperspectral Imagery," *Proc. of SPIE* **3071**, *Algorithms for Multispectral, and Hyperspectral Imagery III*, pp. 61-72, 1997.
3. J. Kerekes, J. Baum, K. Farrar, "Analytical Model of Hyperspectral System Performance," *Proc. of SPIE* **3701**, *Infrared Imaging Systems: Design, Analysis, Modeling, and Testing X*, pp. 155-166, 1999.

4. Berk, A, L.S. Bernstein, G.P. Anderson, P.K. Acharya, D.C. Robertson, J.H. Chetwynd, and S.M. Adler-Golden, "MODTRAN Cloud and Multiple Scattering Upgrades with Application to AVIRIS." *Remote Sens. Environ*., **65**, 367-375, 1998.
5. M.K. Griffin, J.P. Kerekes, K.E. Farrar, H.-h.K. Burke, "Characterization of Gaseous Effluents from Modeling of LWIR Hyperspectral Measurements*," Proc. of SPIE* **4381***, Algorithms for Multispectral, Hyperspectral, and Ultraspectral Imagery VII*, 2001.
6. J.H. Novak and D.B. Turner, "An Efficient Gaussian-Plume Multiple-Source Air Quality Algorithm*," J. Air Pollution Control Association*, **26**(6), 1976.
7. G.A. Briggs, "Diffusion Estimation for Small Emissions," *USAEC report ATDL-106,* U.S. Atomic Energy Commission, Oak Ridge, TN, 1974.
8. F. Pasquill, "Atmospheric Dispersion Parameters in Gaussian Plume Modeling. Part II. Possible Requirements for Change in the Turner Workbook Values," *EPA-600/4-76-030b*, U.S. Environmental Protection Agency, Research Triangle Park, NC, 1976.
9. J.S. Irwin, "A Theoretical Variation of the Wind Profile Law Exponent as a Function of Surface Roughness and Stability," *Atmos. Environ*. **13**, pp. 191-194, 1979.
10. Snell, H.E., G.P. Anderson, J. Wang, J.-L. Moncet, J.H. Chetwynd, and S.J. English, "Validation of FASE (FASCODE for the Environment) and MODTRAN3: Updates and Comparisons with Clear-Sky Measurements." *Proceedings of Passive Infrared Remote Sensing of Clouds and the Atmosphere III*, SPIE **2578**, Orlando, FL, 194-204, 1995.
11. J.A. Hackwell, et al, "LWIR/MWIR Imaging Hyperspectral Sensor for Airborne and Ground-Based Remote Sensing," *Proc. of SPIE* **2819***, Imaging Spectrometry*, 1996.
12. D.R. Hearn, "Fourier Transform Interferometry", *Technical Report 1053*, Lincoln Laboratory, Massachusetts Institute of Technology, Lexington, MA, 02420, 1999.